



Power Electronic Systems
Laboratory

© 2018 IEEE

Proceedings of the International Power Electronics Conference (ECCE Asia 2018), Niigata, Japan, May 20-24, 2018

A Bearingless Synchronous Reluctance Slice Motor with Rotor Flux Barriers

T. Holenstein,
T. Nussbaumer,
J. W. Kolar

Personal use of this material is permitted. Permission from IEEE must be obtained for all other uses, in any current or future media, including reprinting/republishing this material for advertising or promotional purposes, creating new collective works, for resale or redistribution to servers or lists, or reuse of any copyrighted component of this work in other works.



Eidgenössische Technische Hochschule Zürich
Swiss Federal Institute of Technology Zurich

A Bearingless Synchronous Reluctance Slice Motor with Rotor Flux Barriers

Thomas Holenstein^{1*}, Thomas Nussbaumer², Johann W. Kolar¹

¹ Power Electronic Systems Laboratory, ETH Zurich, Zurich, Switzerland

² Levitronix GmbH, Zurich, Switzerland

*E-mail: holenstein@lem.ee.ethz.ch

Abstract—This paper presents a bearingless synchronous reluctance slice motor, which contains no permanent magnets. The rotor with four iron poles and flux barriers is levitated and rotated through a stator winding system with six coils wired as two three-phase systems. After applying a constant rotor oriented magnetization current, the system can be controlled just like a bearingless permanent magnet synchronous slice motor, including the passive stabilization of axial and tilting movements. In a first step, the motor geometry is being optimized and the performance characteristics of the designed motor are examined. The motor is then compared to two other designs, which contain permanent magnets either in the rotor or the stator. The comparison includes torque generation, radial force generation, passive axial and tilting stiffnesses and wide air gap suitability. The introduced topology outperforms the others for ultra high process or ambient temperatures and rotor disposable applications with a short exchange interval.

Keywords—bearingless slice motors, synchronous reluctance motor, topology comparison, wide air gap machines

I. INTRODUCTION

Bearingless motors feature magnetically levitated rotors, and a magnetically integrated bearing function [1]. The same iron circuit is used for torque and radial force generation, with either a separated or a combined winding system. If the stator and rotor lengths are chosen to be much smaller than the rotor diameter, as for the so-called slice motor, only two radial degrees of freedom remain to be actively stabilized apart from the rotation [2].

A significant advantage of bearingless slice motors is that the rotor can be completely separated and isolated from the stator in a simple manner. Contactless rotation in its own containment is possible in the widest range of environmental conditions, which makes these motors perfect for ultra-pure, low shear fluid handling, harsh environmental conditions such as aggressive chemicals, abrasive media or extreme ambient temperatures. To take full advantage, a thick, pressure, heat, and chemistry resistant process chamber wall is needed between the stator and the rotor, requiring a wide air gap in the range of several millimeters. A schematical drawing of such an arrangement is given in Fig. 1.

Many conventional motor topologies can also be configured as bearingless motors [3]. For this reason, bearingless motors have undergone similar evolution since their first demonstration as mechanically supported electrical machines, just with a delay of several years due to the

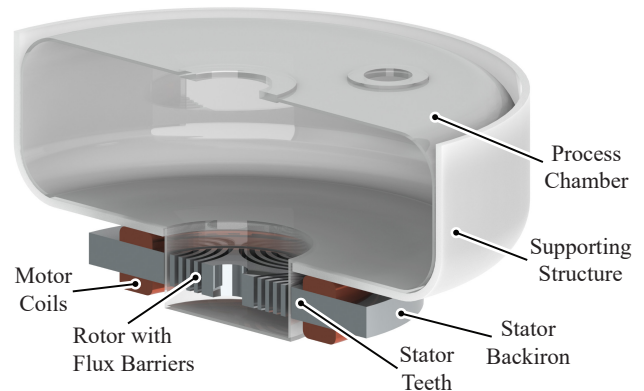


Fig. 1. Bearingless synchronous reluctance slice motor with flux barriers in a process environment.

added complexity. Bearingless induction and reluctance motors were initially demonstrated around 1990 [4], and superseded by rotor permanent magnet (PM) topologies [5], as soon as strong permanent magnet materials became widely available. More recent research has also demonstrated stator-PM topologies [6].

Modern simulation and inverter technologies have led to a reconsideration of synchronous reluctance motors (SynRM) [7]. This development was also driven by the rare-earth price rally in 2011 and has led to commercially available magnet free motors, e.g. from ABB and Siemens. These motors feature rotor flux barriers and achieve competitive efficiencies (IE4, super-premium efficiency level class) [8].

Bearingless SynRM with flux barriers were first introduced in [9]. Linear torque and force generation with much smaller fluctuations over the rotor angle was observed, when compared to reluctance topologies with salient rotor poles. In addition, almost no coupling between force and torque generation exists, which allows to obtain stable bearing operation without a decoupling control algorithm such as needed for salient-pole topologies.

Therefore, it is expected, that such a machine is relatively easy to control, with control algorithms being identical to those of a rotor-PM machine. The only modification needed is to set a constant magnetization current $i_{\text{mag}} = i_{\text{drv,d}}$, which is zero for rotor-PM machines. A variety of recent works deal with the bearingless operation of SynRM with flux barriers [10]–[14].

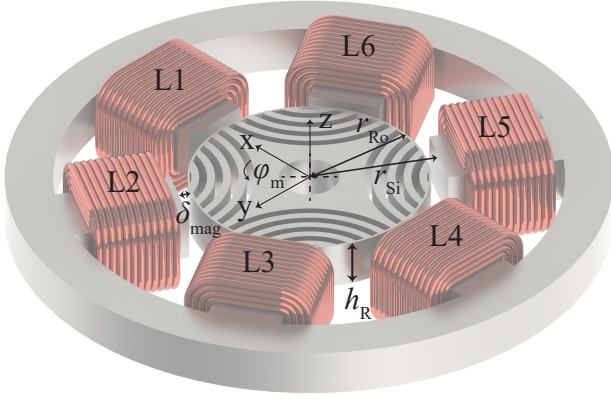


Fig. 2. Introduced bearingless six-slot, four-pole SynRM slice motor with rotor flux barriers and six concentrated motor windings for combined torque and radial force generation.

The main focus of this paper lies on bearingless slice motor topologies without PMs in the rotor featuring a wide air gap. The omission of PMs in the rotor is advantageous for very high ambient temperatures, high rotational speeds, and low manufacturing costs of the rotor. A bearingless flux-switching permanent magnet (FSPM) slice motor was presented in an earlier publication [15]. Despite featuring high torque, several disadvantages regarding the bearing operation were described, namely small radial startup distance as well as strong coupling and angle dependency of the force generation, which required additional control algorithms.

These disadvantages can be mitigated with the SynRM slice motor topology with flux barriers presented in this paper, at the cost of slightly lower torque. The introduced topology is explained in detail in the first part of the paper. A special focus is set on aspects specific to slice motors, namely passive axial and tilting stabilization. A thorough comparison to two other topologies with either permanent magnets in the rotor or the stator is presented in the second part of the paper. Advantageous applications for each of the three topologies are pointed out. Finally, topics of further research are indicated.

II. SYNCHRONOUS RELUCTANCE SLICE MOTOR

A. Motor Design

The introduced bearingless synchronous reluctance slice motor topology with rotor flux barriers is shown in Fig. 2. A four-pole reluctance rotor with four flux barriers per pole is used. All flux barriers are circular and concentric. Six stator teeth, each with a concentrated motor winding for combined torque and radial force generation are used. The stator teeth are connected by a circular back-iron.

In order to accommodate a pressure, heat, and chemistry resistant process chamber wall in the air gap in a later stage, an air gap thickness δ_{mag} to rotor outer radius r_{Ro} ratio G , as defined in (1), of 0.1 is used. This is in line with existing rotor-PM bearingless motor topologies [16]. Note that the terminology "magnetic gap" [17] can

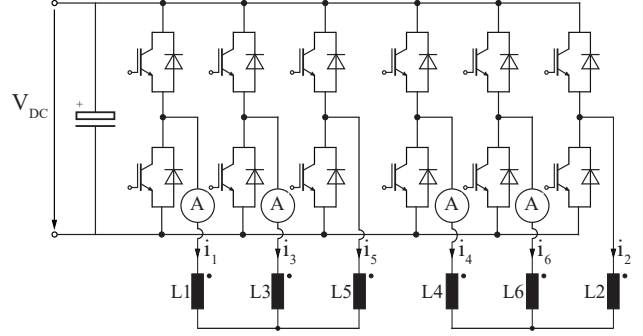


Fig. 3. Connection scheme of the six motor windings to the employed six-phase inverter.

be used interchangeably for "air gap", since all materials inside the gap, namely the fluid and process chamber wall, have a relative permeability μ_r very close to that of air.

$$G = \frac{\delta_{\text{mag}}}{r_{\text{Ro}}} = \frac{r_{\text{Si}}}{r_{\text{Ro}}} - 1 \quad (1)$$

Furthermore, the ratio H of rotor height h_{R} to rotor diameter d_{Ro} , as defined in (2), is set to 0.2 to assure that the axial and tilting movement of the rotor are passively stabilized by the magnetic bias field, which is generated by the constant magnetization current i_{mag} .

$$H = \frac{h_{\text{R}}}{d_{\text{Ro}}} = \frac{h_{\text{R}}}{2r_{\text{Ro}}} \quad (2)$$

B. Winding Layout and Current Generation

The six motor windings are connected as two three-phase systems with a floating star point each and are powered by a six-phase inverter, as shown in Fig. 3. This arrangement is commonly used (see e.g. [18]), leaves four degrees of freedom to be controlled, and requires four current sensors in the inverter to control all currents, since $i_1 + i_3 + i_5 = 0$ and $i_4 + i_6 + i_2 = 0$ holds.

The four degrees of freedom are used to control the radial position in x and y direction, the rotational speed ω_{m} and the magnetization current i_{mag} . A superimposed control algorithm is used to generate setpoint values for the virtual bearing and drive currents $i_{\text{bng},x}$, $i_{\text{bng},y}$, and $i_{\text{drv},q}$, which are directly proportional to the radial forces F_x , F_y and the motor torque T_{m} for a given magnetization current $i_{\text{mag}} = i_{\text{drv},d}$.

Equations (3) and (4) show how these virtual bearing and drive currents are transformed and added to generate the six combined motor winding currents i_1 to i_6 . The rotor angle φ_{m} , rotor pole-pair number $p_{\text{drv}} = 2$, and bearing pole-pair number p_{bng} are used for this transformation and Fig. 2 shows the corresponding coordinate system. For bearingless reluctance motors the relation $p_{\text{bng}} = p_{\text{drv}} \pm 1$ has to hold.

A pole-pair number $p_{\text{bng}} = p_{\text{drv}} - 1 = 1$ is used, since $p_{\text{bng}} = 3$ would exhibit single-phase characteristics with

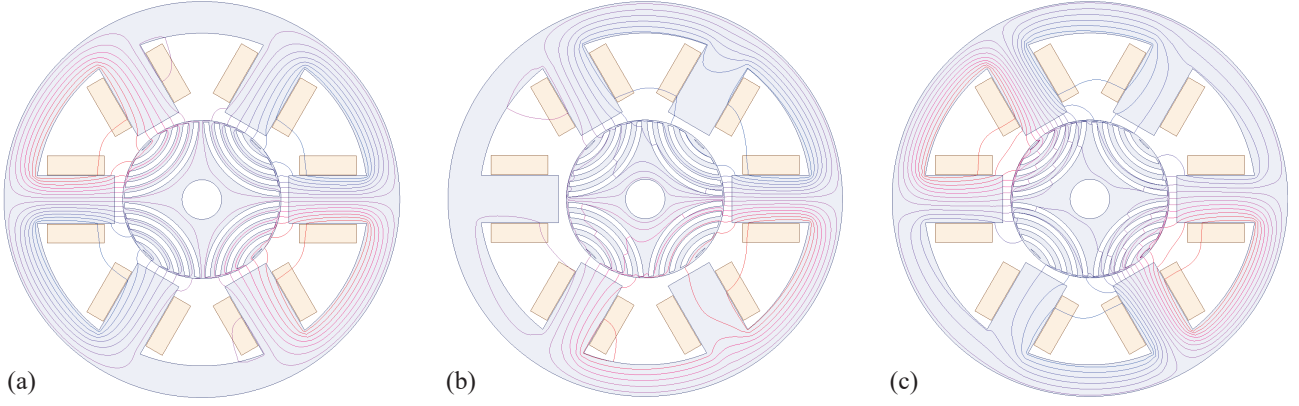


Fig. 4. Bearingless SynRM with field lines shown for: (a) magnetization current ($i_{\text{mag}} = 2000 \text{ AT}$), (b) radial force generation ($i_{\text{mag}} = i_{\text{bng},x} = 2000 \text{ AT}$), (c) torque generation ($i_{\text{mag}} = i_{\text{drv},q} = 2000 \text{ AT}$).

six stator teeth, i.e. it would not be possible to generate radial forces at all rotor angles.

It has to be noted that the winding layout and connection scheme described in this subsection, as well as the motor winding current generation formula

$$\begin{bmatrix} i_1 \\ i_2 \\ i_3 \\ i_4 \\ i_5 \\ i_6 \end{bmatrix} = K(p_{\text{drv}}) \cdot \begin{bmatrix} i_{\text{drv},d} \\ i_{\text{drv},q} \end{bmatrix} + K(p_{\text{bng}}) \cdot \begin{bmatrix} i_{\text{bng},x} \\ i_{\text{bng},y} \end{bmatrix}, \quad (3)$$

where

$$K(p) = \begin{bmatrix} \cos(p_{\text{drv}}\varphi) & \cos(p_{\text{drv}}\varphi + \frac{\pi}{2}) \\ \cos(p_{\text{drv}}\varphi - p\frac{\pi}{3}) & \cos(p_{\text{drv}}\varphi - p\frac{\pi}{3} + \frac{\pi}{2}) \\ \cos(p_{\text{drv}}\varphi - p\frac{2\pi}{3}) & \cos(p_{\text{drv}}\varphi - p\frac{2\pi}{3} + \frac{\pi}{2}) \\ \cos(p_{\text{drv}}\varphi - p\frac{3\pi}{3}) & \cos(p_{\text{drv}}\varphi - p\frac{3\pi}{3} + \frac{\pi}{2}) \\ \cos(p_{\text{drv}}\varphi - p\frac{4\pi}{3}) & \cos(p_{\text{drv}}\varphi - p\frac{4\pi}{3} + \frac{\pi}{2}) \\ \cos(p_{\text{drv}}\varphi - p\frac{5\pi}{3}) & \cos(p_{\text{drv}}\varphi - p\frac{5\pi}{3} + \frac{\pi}{2}) \end{bmatrix} \quad (4)$$

holds for all numbers of rotor pole pairs, as well as for PM-rotor topologies with and without stator teeth (with $i_{\text{mag}} = i_{\text{drv},d} = 0$), as long as a stator with six combined motor windings is used. For FSPM only a very small modification to the matrix $K(p)$ is necessary, as is shown in Section III. Pole pair number and topology configurations can easily be adjusted in software.

In Fig. 4 the field lines in the bearingless SynRM are shown for the three scenarios of magnetization current only (a), radial force generation (b) and torque generation (c). It can be seen that the flux density inside the stator teeth is almost perfectly proportional to the applied current. The field lines do not have to cross the flux barriers for a pure magnetization current. Crossing of the flux barriers results in a reluctance torque.

C. Passive Stabilization, Radial Force, and Torque

A simplified rectangular magnetic circuit with constant cross sectional area A_{fe} , iron length l_{fe} , two air gaps with length l_{δ} , and a coil with n windings wound around the iron carrying a current i is considered. If it is further assumed that there is no stray flux and that the field lines cross the air gap with the same cross section as the iron circuit ($A_{\text{fe}} = A_{\delta}$), the following relationship between magnetomotive force ni (MMF in ampere turns AT) and the B- and H-fields is obtained:

$$\oint H \cdot ds = l_{\text{fe}}H_{\text{fe}} + 2l_{\delta}H_{\delta} = l_{\text{fe}}\frac{B}{\mu_0\mu_r} + 2l_{\delta}\frac{B}{\mu_0} = ni. \quad (5)$$

Solving (5) for B and assuming infinite permeability of the iron, it can be seen that the B-field is proportional to the coil current divided by the air gap length:

$$B = \mu_0 \frac{ni}{\frac{l_{\text{fe}}}{\mu_r} + 2l_{\delta}} \approx \mu_0 \frac{ni}{2l_{\delta}}. \quad (6)$$

The force acting on the two air gaps is proportional to B^2 (7), and therefore, according to (6) also to i^2 (for more details, refer to e.g. [19], Chapter 3)

$$f = \frac{B^2 A_{\text{fe}}}{\mu_0} \approx \frac{\mu_0 A_{\text{fe}} n^2 i^2}{2l_{\delta}^2}. \quad (7)$$

If this simple model is applied to the considered SynRM topology, it can be seen that a magnetization current i_{mag} leads to attracting forces between the stator teeth and the rotor, which increase quadratically with i_{mag} . The sum of all of these forces is zero for a centered rotor due to (3) and (4). For an axial or tilting deflection passive restoring forces are obtained which are pulling the rotor back towards the axial center of the stator. These restoring forces increase linearly with the deflection and stiffness factors k_z , k_{α} , and k_{β} can be defined for a given value of i_{mag} .

For a radial deflection, a negative, unstable force pulling the rotor away from the stator center is obtained

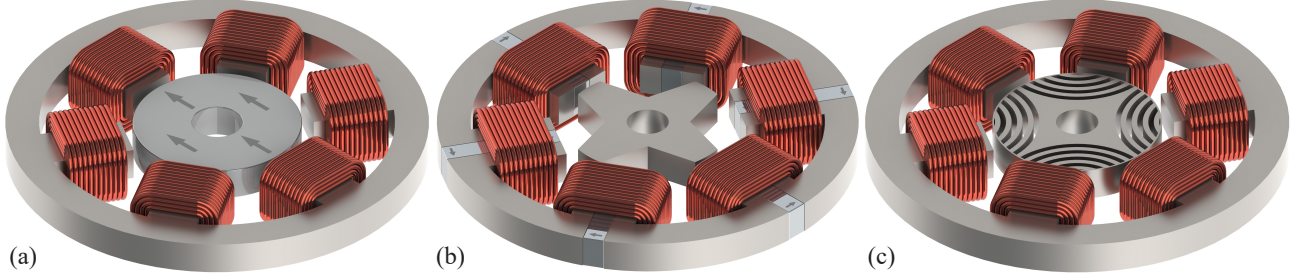


Fig. 5. Compared topologies: (a) bearingless six-slot, two-pole rotor permanent magnet motor (PMSM), (b) bearingless six-slot, four-pole pair flux switching permanent magnet (FSPM) motor, (c) bearingless six-slot, four-pole synchronous reluctance slice motor (SynRM).

and the stiffness factor k_r can be defined accordingly for a given value of i_{mag} .

Considering the motor torque it has to be noted however, that torque increases linearly with $i_{\text{drv},q}$ and also $i_{\text{drv},d}$ as can be seen from the reluctance motor torque equation

$$T = \frac{3}{2} p_{\text{drv}} (L_d - L_q) i_{\text{drv},d} \cdot i_{\text{drv},q}. \quad (8)$$

Radial forces increase linearly with i_{bng} and i_{mag} as well, which is best illustrated by the forces of two opposing stator teeth being added to form the resulting radial force, e.g. $F_{x,1} = F_{\text{coil}1} + F_{\text{coil}2}$ at $\varphi_m = 0$ deg yielding

$$F_{x,1} \propto (i_{\text{mag}} + i_{\text{bng},x})^2 - (i_{\text{mag}} - i_{\text{bng},x})^2 = 4i_{\text{mag}}i_{\text{bng},x}. \quad (9)$$

For slice motors with a wide air gap as in the considered case, the simple model assumption of having no stray flux and straight field lines within the air gap does not hold true any more. Considerable stray flux paths between the stator teeth as well as below and above the motor exist. This leads to a higher than expected B-field magnitude in the iron below the coils and a lower than expected B-field magnitude within the air gap and the rotor. In other words, saturation occurs earlier than expected and forces are lower than expected. For this reason, 3D FEM simulations are carried out to obtain the absolute values of the expected forces and the torque. Nevertheless, the proportionality relations of the simple model hold true.

D. Magnetization Current Considerations

Due to the quadratic relation between the total current and forces as well as torque, respectively, the SynRM topology performs better compared to PM topologies for a high MMF. For this reason, a very high MMF of several thousand AT was chosen for the simulations, for which the stator is already partly saturated. Torque simulations were performed at a drive current angle of 45 deg, since the maximum torque per total current is achieved for $i_{\text{mag}} = i_{\text{drv},d} = i_{\text{drv},q}$. Therefore, the magnetization current was set to $i_{\text{mag}} = MMF/\sqrt{2}$, which causes the ohmic idle losses to be half of the full load losses. It has

to be noted that generating such high MMF constantly will most likely require advanced water cooling for the stator coils. In this paper the notation $\hat{A}T$ was used for a $MMF/\sqrt{2}$.

Having a completely firmware-adjustable magnetization current for a bearingless slice motor provides several new possibilities unknown to PM topologies, namely:

- Adjustable axial steady-state position
- Improved damping of axial oscillations compared to PM motors (e.g. [20])
- Avoidance of resonances during run up, through dynamic stiffness adjustment
- Dynamic prioritization between high dynamics and low iron losses for high speed operation.

These items provide a variety of research topics once a bearingless SynRM prototype is available, and are expected to open new opportunities and applications.

III. PERMANENT MAGNET TOPOLOGIES FOR COMPARISON

To put the performance of the introduced SynRM topology into perspective, it is compared to two other topologies with PMs either in the rotor or the stator. All three topologies are shown in Fig. 5. Identical rotor diameters as well as ratios for G and H according to (1) and (2) respectively, are used for all three topologies. All topologies have six stator teeth, each with a concentrated motor winding for combined torque and force generation.

The rotor permanent magnet synchronous motor (PMSM) topology features a diametrically-magnetized two-pole rotor with identical current generation to the SynRM topology as described in (3) and (4), using $p_{\text{pmsm},\text{drv}} = 1$, $p_{\text{pmsm},\text{bng}} = 2$, the same coordinate system as in Fig. 2, and setting $i_{\text{pmsm},\text{mag}} = i_{\text{pmsm},\text{drv},d} = 0$.

The stator PM topology is an FSPM motor with four rotor teeth. Each stator tooth contains a tangentially-magnetized PM with alternating magnetization direction. For the current generation the coordinate system from Fig. 2 and (3) with $p_{\text{fspm},\text{drv}} = 4$ and $p_{\text{fspm},\text{bng}} = 5$ are used. However, the matrix K needs to be slightly modified as shown in (10), since alternating current directions due

to the alternating PM bias flux are required, and a rotor tooth in front of an energized stator tooth experiences a tangential instead of a radial force. Due to the fact that mostly tangential forces are generated, this topology is very effective at generating torque, but less effective for generating bearing forces (see e.g. [15]), since both radial and tangential forces are used to generate bearing forces.

$$K_{\text{fspm}}(p) = \begin{bmatrix} \cos(p_{\text{drv}}\varphi + \frac{\pi}{2}) & \cos(p_{\text{drv}}\varphi + \pi) \\ \cos(p_{\text{drv}}\varphi - p\frac{\pi}{3} - \frac{\pi}{2}) & \cos(p_{\text{drv}}\varphi - p\frac{\pi}{3}) \\ \cos(p_{\text{drv}}\varphi - p\frac{2\pi}{3} + \frac{\pi}{2}) & \cos(p_{\text{drv}}\varphi - p\frac{2\pi}{3} + \pi) \\ \cos(p_{\text{drv}}\varphi - p\frac{3\pi}{3} - \frac{\pi}{2}) & \cos(p_{\text{drv}}\varphi - p\frac{3\pi}{3}) \\ \cos(p_{\text{drv}}\varphi - p\frac{4\pi}{3} + \frac{\pi}{2}) & \cos(p_{\text{drv}}\varphi - p\frac{4\pi}{3} + \pi) \\ \cos(p_{\text{drv}}\varphi - p\frac{5\pi}{3} - \frac{\pi}{2}) & \cos(p_{\text{drv}}\varphi - p\frac{5\pi}{3}) \end{bmatrix} \quad (10)$$

It has to be noted that the usage of stator PMs, both for a homopolar and multipolar stator-PM bias flux, doubles p_{drv} for the same rotor geometry compared to a SynRM. Each rotor tooth yields identical characteristics in front of the same stator tooth for a given PM stator bias flux. For a SynRM, however, a rotating bias flux is applied, which effectively assigns a positive or negative value to each rotor tooth.

IV. PERFORMANCE COMPARISON

The following performance comparison is carried out with respect to the target application, which requires achieving high rotor torque densities and high passive axial and tilting stiffnesses with wide air gap bearingless slice motors at relatively low rotational speeds (see e.g. [15]).

As such motors are usually thermally limited, torque and active radial forces are compared at the same motor losses, which consist mostly of ohmic winding losses while iron losses can be neglected due to the low rotational speeds. This is achieved for an identical MMF in AT as the winding space is equal. However, to provide the passive stabilization, the SynRM will generate half of these ohmic full-load losses, while the PMSM and FSPM topologies will both generate no ohmic losses.

For the 3D FEM simulations the material properties of neodym-iron-boron magnets in grade N45 and magnetic steel M330-35A were used.

A. Passive Axial and Tilting Stability

Passive stabilization of the axial position z and for the two tilting degrees of freedom, α and β , is achieved with the rotor or stator PMs for the PMSM and the FSPM topology, respectively, while for the introduced SynRM passive stabilization is achieved through the current i_{mag} .

The axial restoring force versus the axial deflection of the rotor is shown in Fig. 6. While the axial stiffness

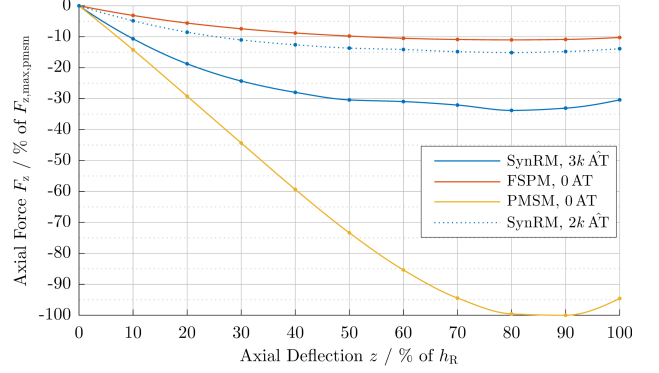


Fig. 6. Passive axial restoring force F_z vs. axial deflection z .

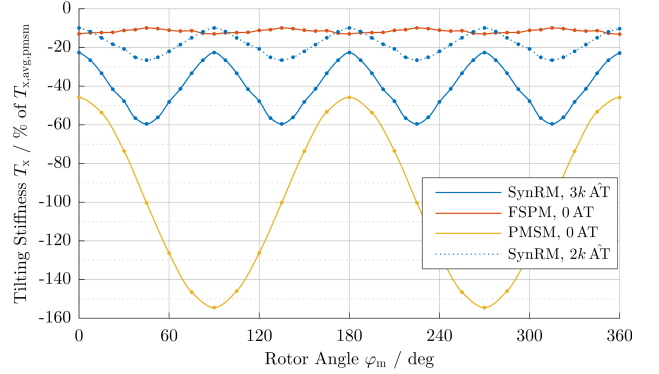


Fig. 7. Passive tilting stiffness T_x vs. rotor angle φ_m .

as described by (11) is linear for the PMSM up to approximately 50% of deflection, it decreases immediately for the two other topologies. Table I summarizes the maximum axial stiffness $k_{z,\text{max}}$, maximum axial load $F_{z,\text{max}}$, and the axial equilibrium deflection z_{equ} (11) for all three topologies. The axial equilibrium position results from gravity ($g = 9.81 \frac{\text{m}}{\text{s}^2}$) acting on the rotor of the horizontally-oriented motor, where the relative rotor densities ($\rho_{v,\text{pmsm}} = 91.0\%$, $\rho_{v,\text{fspm}} = 53.6\%$, $\rho_{v,\text{synrm}} = 59.8\%$), material densities ($\rho_{m,\text{ndfeb}} = 7.5 \frac{\text{g}}{\text{cm}^3}$, $\rho_{m,\text{m330}} = 7.65 \frac{\text{g}}{\text{cm}^3}$), and axial restoring forces from Fig. 6 have been used.

$$k_z = \frac{dF_z}{dz} \quad \text{and} \quad z_{\text{equ}} : F_{z,\text{equ}} = -F_g \quad (11)$$

It should be noted that the following simulations, for which the results are shown in Fig. 7 - 12, do not include the performance degradation due to the axial equilibrium deflection, since the influence would be small and dependent on the mounting orientation and additional rotor load.

TABLE I. AXIAL AND TILTING PERFORMANCE

	PMSM	FSPM	SynRM 2k AT	SynRM 3k AT
$k_{z,\text{max}}$	100%	20.7%	32.2%	70.8%
$F_{z,\text{max}}$	100%	11.0%	15.1%	33.8%
z_{equ}	7.5%	22.0%	15.2%	6.3%
$k_{\alpha,\beta,\text{avg}}$	100%	11.5%	18.3%	41.1%

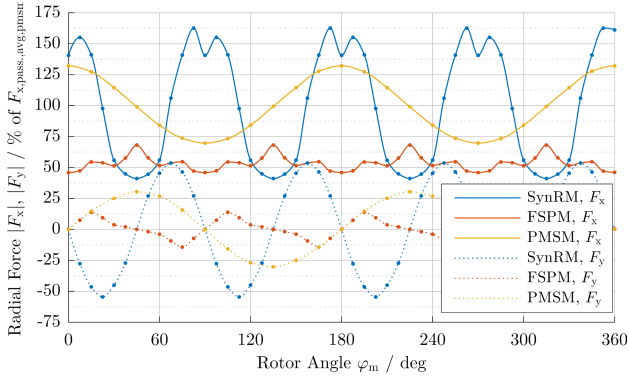


Fig. 8. Passive radial forces F_x and F_y for a deflection in x direction of 40% of the air gap δ_{mag} . SynRM with $i_{\text{mag}} = 2k \text{ AT}$.

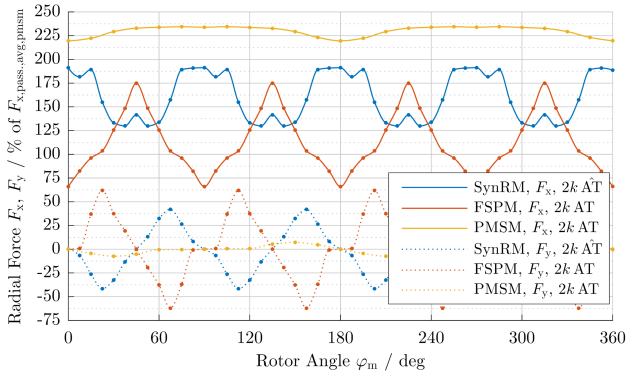


Fig. 9. Active radial forces F_x and F_y generated by current $i_{\text{bng},x}$.

The passive tilting stiffness versus the rotor angle is shown in Fig. 7 and summarized in Table I. It can be seen how the difference between the weak α -axis and the strong β -axis is very pronounced for small pole pair numbers (i.e. the PMSM), while it is almost negligible for the FSPM topology. A big difference between $k_\alpha = dT_\alpha/d\alpha$ and $k_\beta = dT_\beta/d\beta$ can be problematic for low rotational speeds, since the tilting eigenfrequencies are excited just from having an initial tilting deflection, e.g. through disturbance forces.

B. Radial Forces and Torque

Destabilizing passive radial forces for a radially deflected rotor are shown in Fig. 8. Active radial forces for a centered rotor are shown in Fig. 9. In order to safely achieve radial startup when the motor is switched on, the active forces need to be larger than the passive destabilizing forces at any rotor angle φ_m , as can be seen in (12). This startup condition is satisfied for all three topologies for $x = 0.4 \cdot \delta_{\text{mag}}$ and $i_{\text{bng}} = 2k \text{ AT}$ with varying margins.

$$k_x(\varphi_m) \cdot x < k_i(\varphi_m) \cdot i_{\text{bng},x} \quad \forall \varphi_m \quad (12)$$

The angle deviation of the radial force is shown in Fig. 10. The deviation is almost zero for the PMSM and quite large for the FSPM at ± 30 deg, as expected. For the SynRM it is significantly larger than expected at ± 15 deg.

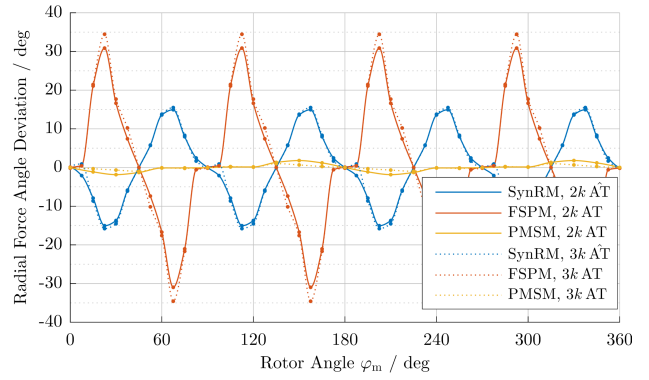


Fig. 10. Radial force angle deviation from x for a current $i_{\text{bng},x}$.

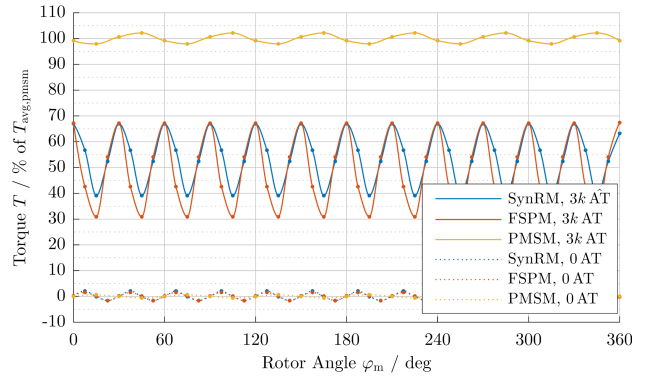


Fig. 11. Torque generation including cogging torque vs. rotor angle.

In [9], a stability range of ± 5 deg is given for the bearing control, which is considered to be rather conservative, but for ± 15 deg a decoupling controller is most likely required.

Additional investigations have shown that the stator slot number of six is the root cause for this angle deviation. For a stator with twelve slots (or 24 as in [9]), the same rotor shows constant force and torque generation over φ_m and almost no angle deviation similar to the PMSM topology. However, a stator with twelve slots and a four-pole rotor exhibit a poor winding factor for concentrated coils and would also require separate force and torque windings, since combined torque and force generation would not be possible with a power converter consisting of six half bridges.

Torque generation, including the cogging torque, for all three topologies is shown in Fig. 11. The torque generation for different air gap ratios G is shown in Fig. 12, which reveals that the performance of the PMSM scales with a different exponent with regard to the air gap ratio. Therefore, the PMSM topology is much better suited for even larger air gap ratios G compared to the FSPM and SynRM topologies.

Table II summarizes the radial force and torque performance for the three topologies. From the performance increase between an MMF of $2k \text{ AT}$ and $3k \text{ AT}$ a good indication about the average saturation level can be obtained. Without saturation an increase of factor 1.5,

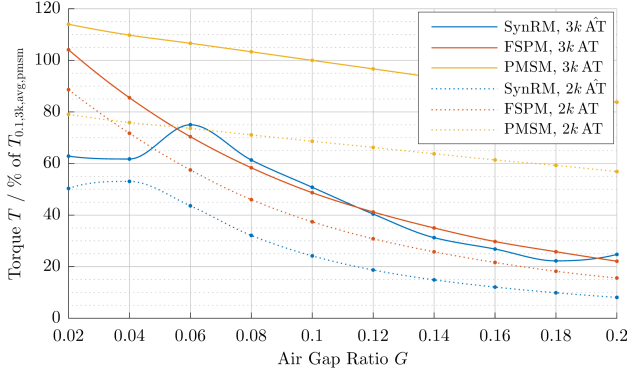


Fig. 12. Torque generation vs. air gap ratio.

TABLE II. RELATIVE RADIAL FORCE AND TORQUE PERFORMANCE

	PMSM	FSPM	SynRM
F_x 2k AT	0.720	0.353	0.502
F_x 3k AT	1.000	0.397	0.845
F_x increase	1.39	1.12	1.30^2
T 2k AT	0.686	0.374	0.242
T 3k AT	1.000	0.487	0.538
T increase	1.46	1.30	1.49^2

respectively 1.5^2 would be expected, which in terms of the torque is almost reached for the SynRM and the PMSM, but not for the FSPM. Therefore, conclusions regarding the maximum torque and force capability can be drawn from constants obtained for small MMF.

The saturation level for radial force generation is generally higher, since the bearing current $i_{bn,g,x}$ and magnetization current i_{mag} (or PM bias flux, respectively) coincide at certain rotor angles φ_m , resulting in an MMF which is higher by a factor of $\sqrt{2}$.

V. CONCLUSION

A bearingless synchronous reluctance slice motor (SynRM) with six stator slots and rotor flux barriers was introduced in this paper. The topology was explained in detail and the basic feasibility of the concept was shown through 3D FEM simulations. The evaluated performance of the PM-free topology was compared to two other topologies with PMs in the stator (FSPM) and the rotor (PMSM), respectively.

Strengths and weaknesses of each topology are summarized in Table III. The application-specific suitability is shown in Table IV. It is clear that PMSMs will remain the best option for general applications. For some special applications, the presented SynRM might, however, be an attractive option. These applications include ultra-high process or ambient temperatures and rotor disposable applications with a short exchange interval.

In a next step the authors are planning to build a prototype of such a bearingless SynRM with rotor flux barriers also to explore the new possibilities of dynamic stiffness adjustments, e.g. for axial position adjustments,

TABLE III. PERFORMANCE COMPARISON: (A) SYNRM, (B) FSPM, (C) PMSM

	(A)	(B)	(C)
Torque Generation Capability	-	+	++
Passive Axial and Tilting Stiffness	-	--	+
Force and Torque Linearity	-	--	++
Expected Power Efficiency	--	-	+
Wide Air Gap Suitability	-	-	++
Manufacturing Cost Rotor	++	++	--
Manufacturing Cost Stator	+	--	++
Rare Earth Independence Rotor	++	++	--
Rare Earth Independence Stator	++	--	++

TABLE IV. APPLICATION SUITABILITY: (A) SYNRM, (B) FSPM, (C) PMSM

	(A)	(B)	(C)
General, Allround	--	--	++
High Speed Rotation	+	-	++
High Process Temperatures	++	+	-
High Ambient Temperatures	++	-	-
Long Usage Rotor Disposable	-	+	+
Short Usage Rotor Disposable	++	+	--

resonance avoidance during run up, or prioritization between performance and iron losses.

REFERENCES

- [1] A. Chiba, T. Fukao, O. Ichikawa, M. Oshima, M. Takemoto, and D. G. Dorrell, *Magnetic bearings and bearingless drives*. Elsevier, 2005.
- [2] S. Silber, W. Amrhein, P. Bösch, R. Schöb, and N. Barletta, "Design aspects of bearingless slice motors," *IEEE/ASME Transactions on Mechatronics*, vol. 10, no. 6, pp. 611–617, Dec. 2005.
- [3] B. Liu, "Survey of bearingless motor technologies and applications," in *Proc. IEEE Int. Conf. Mechatronics and Automation (ICMA)*, Aug. 2015, pp. 1983–1988.
- [4] A. Chiba, T. Deido, T. Fukao, and M. A. Rahman, "An analysis of bearingless AC motors," *IEEE Transactions on Energy Conversion*, vol. 9, no. 1, pp. 61–68, Mar. 1994.
- [5] X. Sun, L. Chen, and Z. Yang, "Overview of bearingless permanent-magnet synchronous motors," *IEEE Transactions on Industrial Electronics*, vol. 60, no. 12, pp. 5528–5538, Dec. 2013.
- [6] W. Gruber, W. Briewasser, M. Rothböck, and R. T. Schöb, "Bearingless slice motor concepts without permanent magnets in the rotor," in *Proc. IEEE Int. Conf. Industrial Technology (ICIT)*, Feb. 2013, pp. 259–265.
- [7] G. Pellegrino, T. M. Jahns, N. Bianchi, W. L. Soong, and F. Cupertino, *The rediscovery of synchronous reluctance and ferrite permanent magnet motors: tutorial course notes*. Springer, 2016.
- [8] J. Estima and A. Cardoso, "Super premium synchronous reluctance motor evaluation," in *Proc. International Conference on Energy Efficiency in Motor Driven Systems (EEMODS)*, 2013, pp. 213–222.
- [9] M. Takemoto, K. Yoshida, N. Itasaka, Y. Tanaka, A. Chiba, and T. Fukao, "Synchronous reluctance type bearingless motors with multi-flux barriers," in *Proc. Power Conversion Conf. - Nagoya*, Apr. 2007, pp. 1559–1564.
- [10] V. Mukherjee, J. Pippuri, S. E. Saarakkala, A. Belahcen, M. Hinkkanen, and K. Tammi, "Finite element analysis for bearingless operation of a multi flux barrier synchronous reluctance motor," in *Proc. 18th Int. Conf. Electrical Machines and Systems (ICEMS)*, Oct. 2015, pp. 688–691.

- [11] S. E. Saarakkala, M. Sokolov, V. Mukherjee, J. Pippuri, K. Tammi, A. Belahcen, M. Hinkkanen *et al.*, "Flux-linkage model including cross-saturation for a bearingless synchronous reluctance motor," in *Proc. of the ISMB15, Kitakyushu, Japan*, 2016.
- [12] H. Ding, H. Zhu, and Y. Hua, "Optimization design of bearingless synchronous reluctance motor," *IEEE Transactions on Applied Superconductivity*, vol. 28, no. 3, Apr. 2018.
- [13] X. Diao, H. Zhu, Y. Qin, and Y. Hua, "Torque ripple minimization for bearingless synchronous reluctance motor," *IEEE Transactions on Applied Superconductivity*, vol. 28, no. 3, Apr. 2018.
- [14] A. Belahcen, V. Mukherjee, F. Martin, and P. Rasilo, "Computation of hysteresis torque and losses in a bearingless synchronous reluctance machine," *IEEE Transactions on Magnetics*, vol. 54, no. 3, Mar. 2018.
- [15] T. Holenstein, J. Greiner, D. Steinert, and J. W. Kolar, "A high torque, wide air gap bearingless motor with permanent magnet free rotor," in *Proc. IEEE Int. Electric Machines and Drives Conf. (IEMDC)*, May 2017.
- [16] J. Asama, T. Tatara, T. Oiwa, and A. Chiba, "Suspension performance of a two-dof actively positioned consequent-pole bearingless motor with a wide magnetic gap," in *Proc. IEEE Int. Electric Machines Drives Conf. (IEMDC)*, May 2015, pp. 786–791.
- [17] H. Sugimoto, Y. Uemura, A. Chiba, and M. A. Rahman, "Design of homopolar consequent-pole bearingless motor with wide magnetic gap," *IEEE Transactions on Magnetics*, vol. 49, no. 5, pp. 2315–2318, May 2013.
- [18] D. Steinert, T. Nussbaumer, and J. W. Kolar, "Slotless bearingless disk drive for high-speed and high-purity applications," *IEEE Transactions on Industrial Electronics*, vol. 61, no. 11, pp. 5974–5986, Nov. 2014.
- [19] H. Bleuler, M. Cole, P. Keogh, R. Larssonneur, E. Maslen, Y. Okada, G. Schweitzer, A. Traxler *et al.*, *Magnetic bearings: theory, design, and application to rotating machinery*. Springer Science & Business Media, 2009.
- [20] H. Sugimoto, M. Miyoshi, and A. Chiba, "Axial vibration suppression by field flux regulation in two-axis actively positioned permanent magnet bearingless motors with axial position estimation," *IEEE Transactions on Industry Applications*, vol. 54, no. 2, pp. 1264–1272, Mar. 2018.